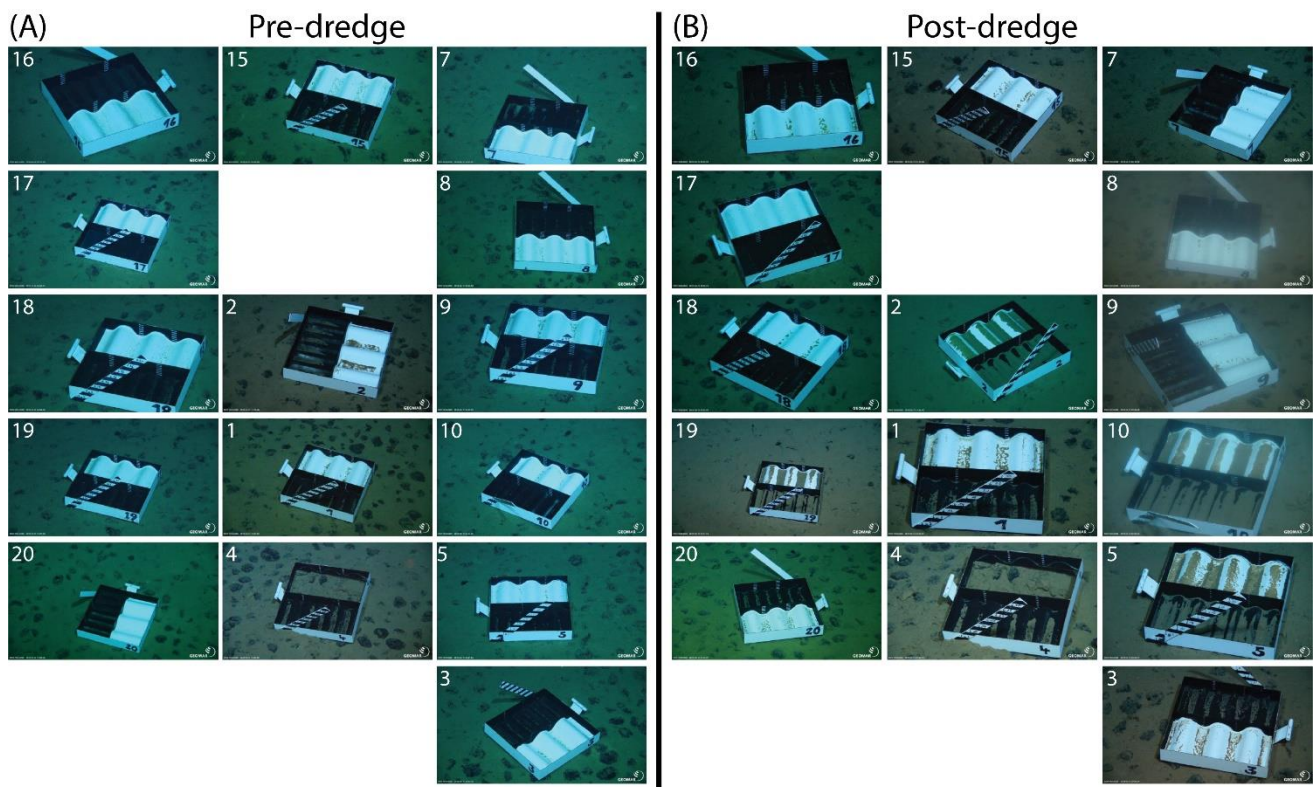


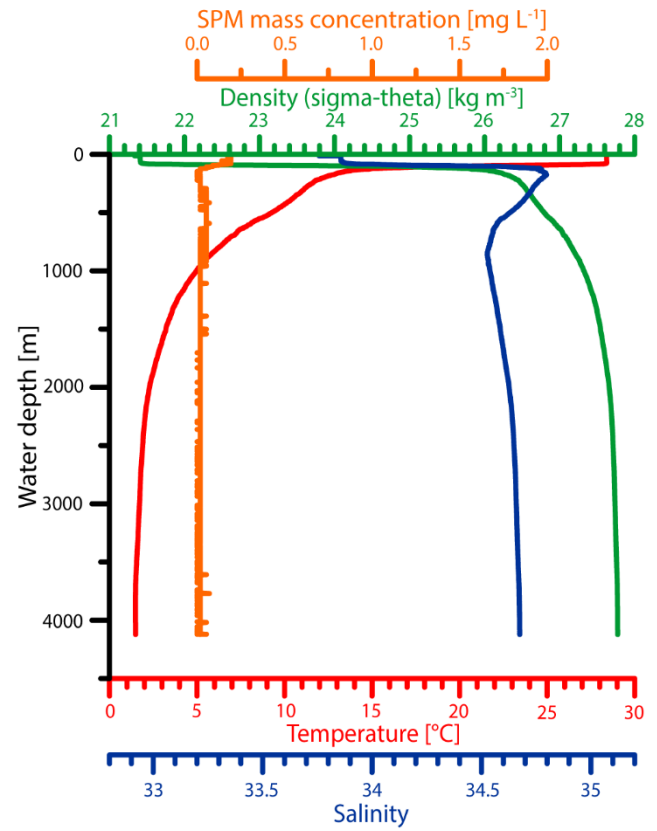
Supplementary Material

Monitoring of anthropogenic sediment plumes in the Clarion-Clipperton Zone, NE equatorial Pacific Ocean

1 Supplementary Figures

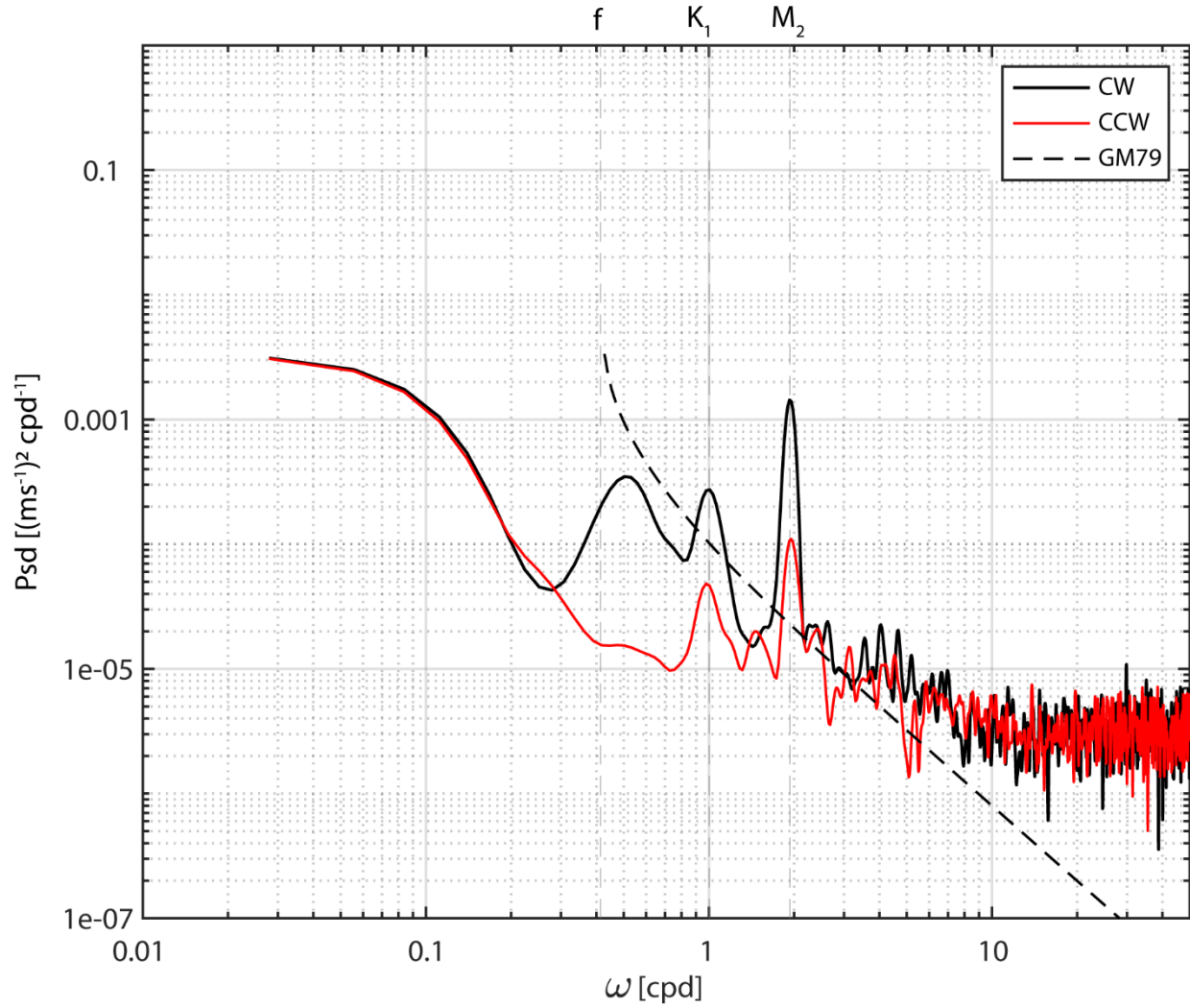


Supplementary Figure 1. (A) Pre-dredge photos of the SLIC boxes. (B) Post-dredge photos of the SLIC boxes. Please note that SLIC box 04 lost its white bottom part, therefore showing the underlying seafloor. Numbers on the top left of the photos show the number of the individual SLIC box. Photo courtesy: GEOMAR, ROV Team Kiel 6000.



Supplementary Figure 2 (left). Onboard calibration setup in the cold lab. Calibration of the OBSs were carried out with lights dimmed (photo courtesy: Henko de Stigter).

Supplementary Figure 3 (right). Water column profiles of temperature (red), salinity (blue), density (green) and SPM mass concentration as inferred from the JFE Advantech OBS (orange) obtained with the CTD in the dredge experiment area (SO268/2-ST208-CTD17).

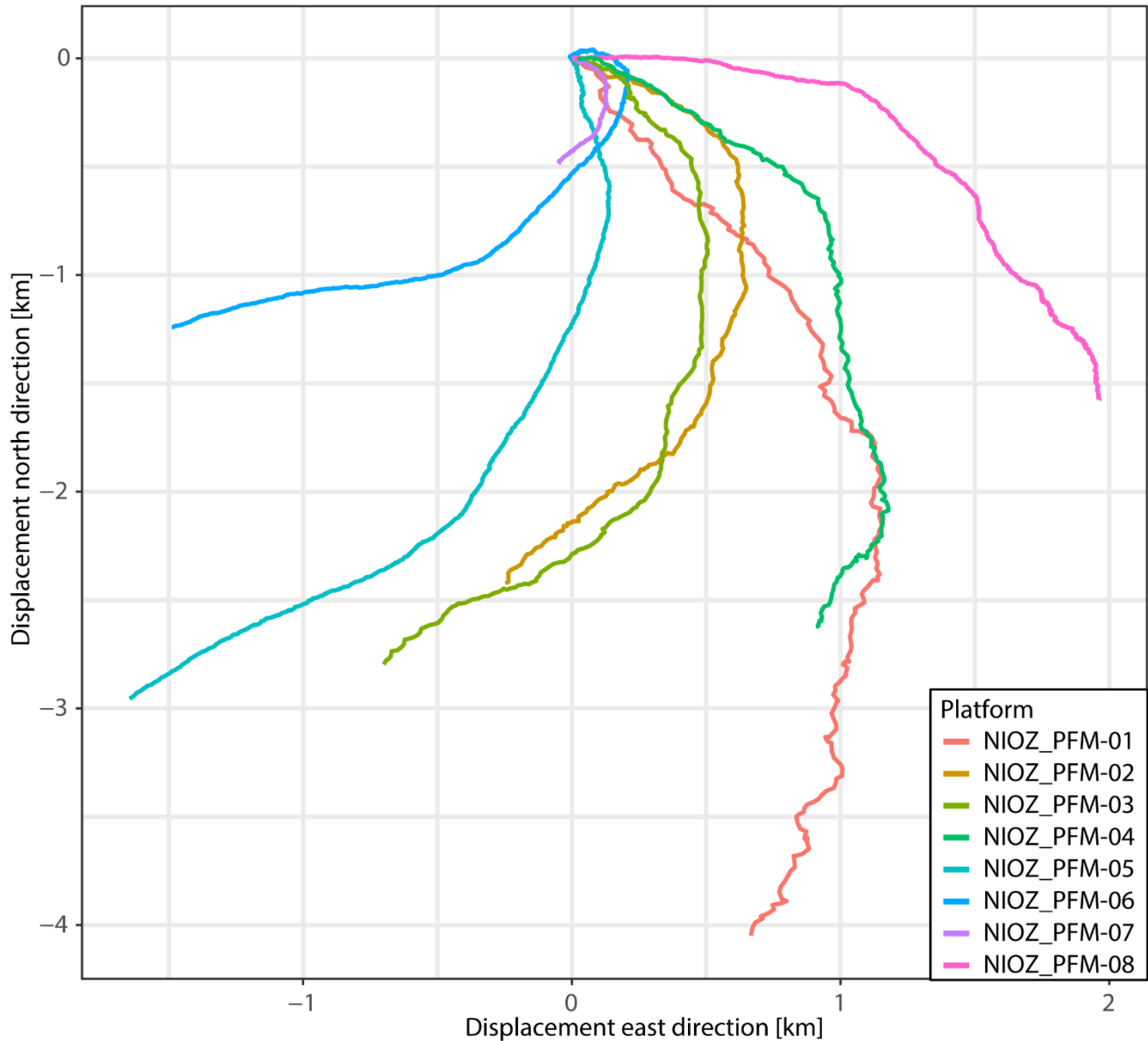


Supplementary Figure 4. Power spectral density (PSD) inferred from the current velocities of bin 3 of the Nortek Aquadopp profilers on NIOZ_PFM-02 from the 9th of April until the 14th of May 2019.

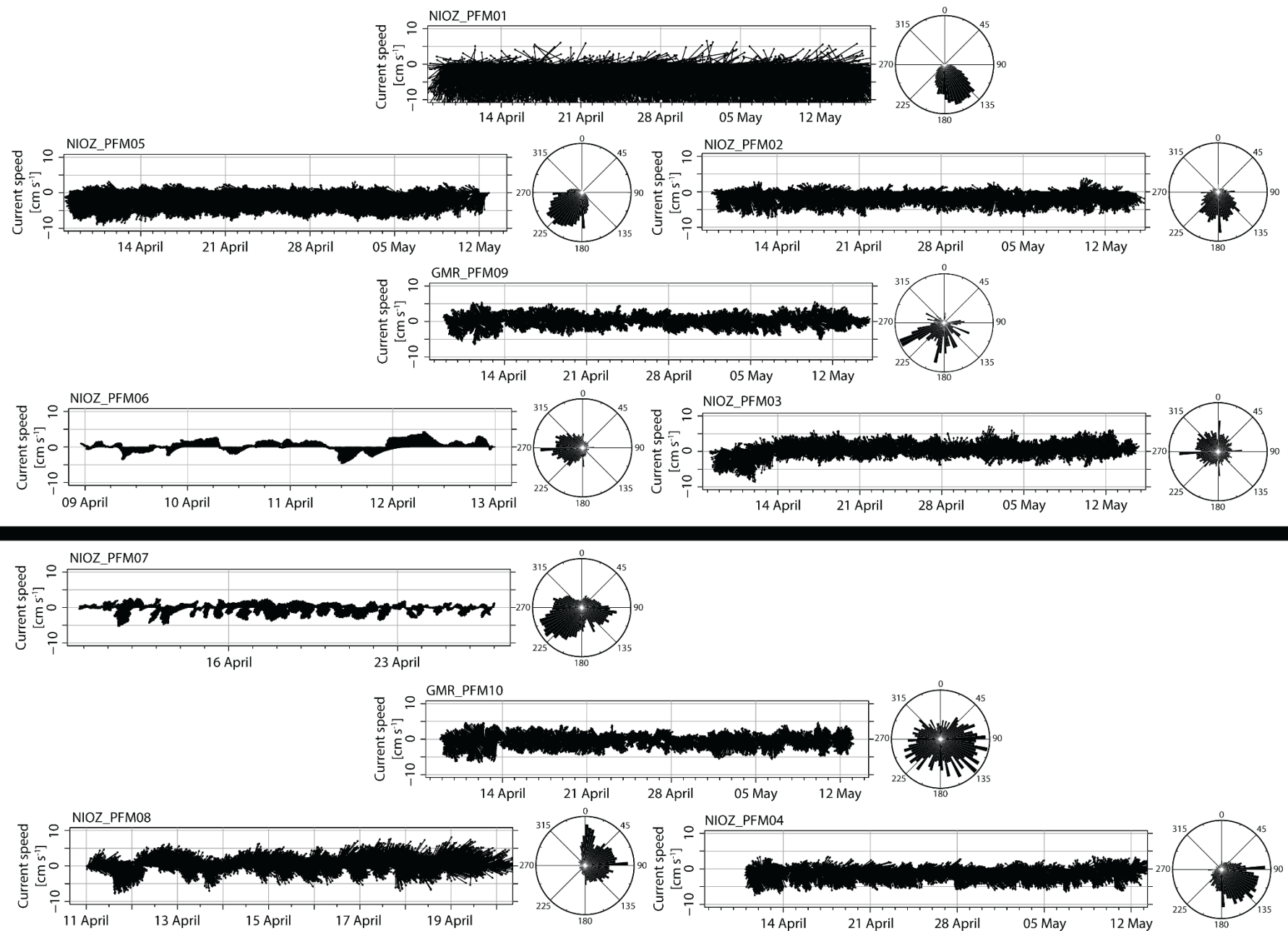
The spectra are calculated from each 5-min segment in order to show the most prominent frequency. The current velocity is considered as a complex rotary velocity vector ($u+iy$) (e.g. Alfrod et al., 2012). The energy spectrums of other sensors at different stations show very similar patterns). The clockwise (CW) and counterclockwise (CCW) rotations relating to negative and positive frequencies are shown by the black and red lines.

Motions at near inertial frequencies are strongly polarized, with clockwise energy around two orders of magnitude larger than counterclockwise energy. Similar differences have been observed in the northern hemisphere in previous studies (Alfrod, 2003). The magnitude of the counterclockwise motion is in good agreement with the Garret and Munk (1972) predictions, except for the high frequency motions, which are most likely attributable to noise in the measurements.

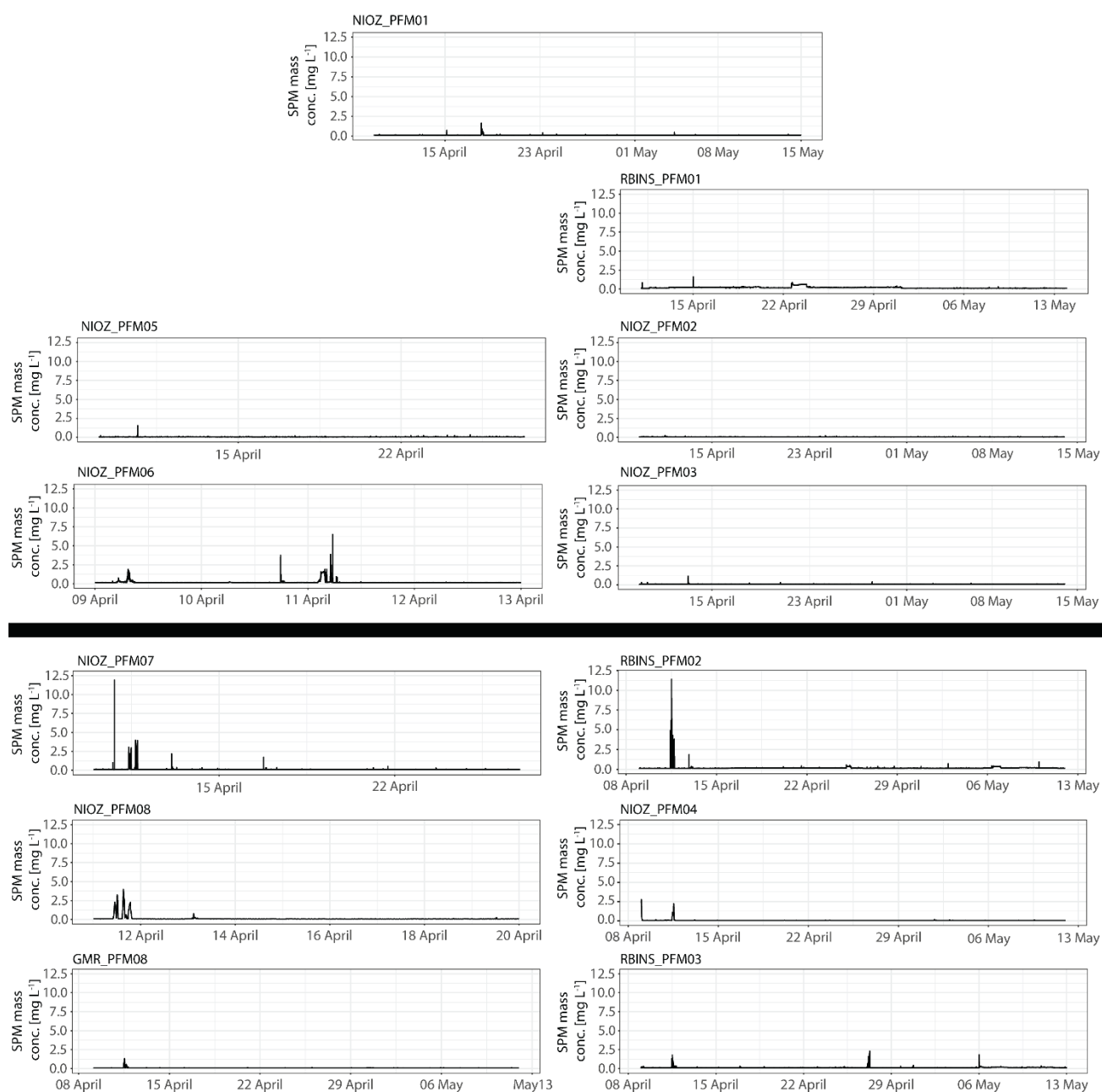
The relatively short time series of data did not allow lower frequency motions to be resolved. The high-frequency motion is dominated by different semidiurnal and diurnal tidal harmonic components M2 and K1. Note that the dominant high-frequency signals are evident in both clockwise and counterclockwise rotations, while the near-inertial oscillation is only depicted in the clockwise rotations. Inertial motion f is well below other dominant frequencies and therefore can be clearly seen. Although an individual peak does not occur at inertial frequency, a wide near-inertial peak results in a remarkable energy content in the data.



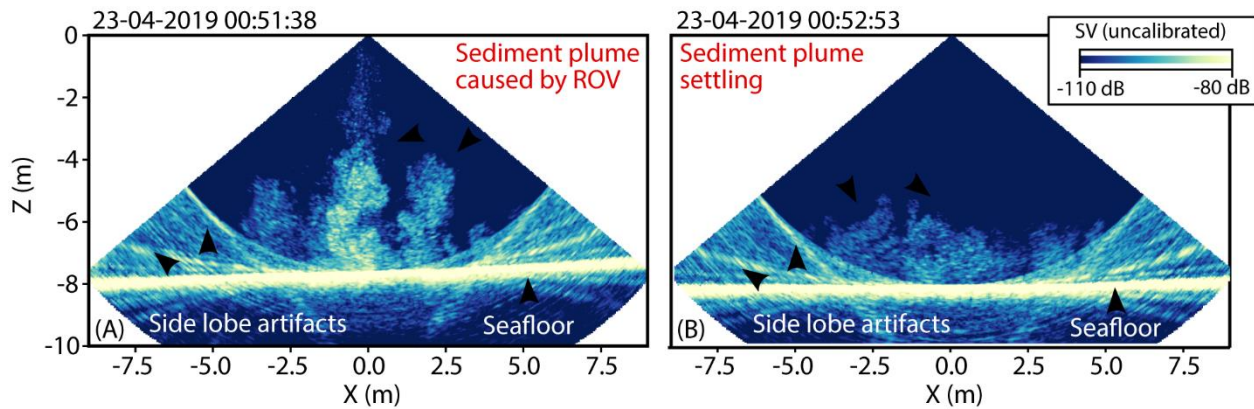
Supplementary Figure 5. Progressive vector diagrams of cumulative water displacement at different sensor platforms between the 11th of April 06:30 UTC and 12th of April 00:00 UTC. The current at SO268/2-NIOZ_PFM-01 was measured at 0.7 mab, at all other NIOZ platforms at 1.25 mab.



Supplementary Figure 6. Feather plots and rose diagrams of current speed and directions as recorded by the Nortek Aquadopp profilers (bin 1 at 1.25 mab, NIOZ_PFM-02 and -08) and RDI workhorse ADCPs (bin 7 at 19 mab, GMR_PFM-09 and -10, bin 3, 0.7 mab, NIOZ_PFM-01) for the entire duration of the deployments. Note that time scales are different, with platforms NIOZ_PFM-06, NIOZ_PFM-07 and NIOZ_PFM-08 having a shorter time span. The arrangement of the time series graphs corresponds with the geographical arrangement of the sensor platforms north and south of the dredge tracks (black line through the centre).



Supplementary Figure 7. Time series of SPM mass concentration as recorded by the OBSs for the entire duration of the deployment. Note that time scales are different, with platforms NIOZ_PFM-05, NIOZ_PFM-06, NIOZ_PFM-07 and NIOZ_PFM-08 represent a shorter time span. The arrangement of the time series graphs corresponds with the geographical arrangement of the sensor platforms north and south of the dredge tracks (black line through the centre).



Supplementary Figure 8. Multibeam images of the lower metres of water column and underlying seafloor showing a sediment plume generated by the thrusters of the ROV. **(A)** Sediment plume extending up to 6 mab. **(B)** Settling of the generated sediment plume 1 minute later.

2 References

- Alford, M. H., 2003. Energy available for ocean mixing redistributed through long-range propagation of internal waves, *Nature*, v. 423, p. 159-163. <https://doi.org/10.1038/nature01628>
- Alford, M. H., Cronin, M. F. and Klymak, J.M., 2012. Annual cycle and depth penetration of wind-generated near-inertial internal waves at ocean station Papa in the Northeast Pacific. *Journal of Physical Oceanography*, v. 42, p. 889-909. <https://doi.org/10.1175/JPO-D-11-092.1>
- Garrett, C. J. and Munk, W., 1972. Space-time scales of internal waves. *Geophysical Fluid Dynamics*, v2, p. 255-264. <https://doi.org/10.1080/03091927208236082>